Magnetic Resonance in Medicine 44:625–632 (2000)

In Vivo Fiber Tractography Using DT-MRI Data

Peter J. Basser,[1*] Sinisa Pajevic,[2] Carlo Pierpaoli,[1] Jeffrey Duda,[1] and Akram Aldroubi[3]

Fiber tract trajectories in coherently organized brain white matter pathways were computed from in vivo diffusion tensor magnetic resonance imaging (DT-MRI) data. First, a continuous diffusion tensor field is constructed from this discrete, noisy, measured DT-MRI data. Then a Frenet equation, describing the evolution of a fiber tract, was solved. This approach was validated using synthesized, noisy DT-MRI data. Corpus callosum and pyramidal tract trajectories were constructed and found to be consistent with known anatomy. The method's reliability, however, degrades where the distribution of fiber tract directions is nonuniform. Moreover, background noise in diffusion-weighted MRIs can cause a computed trajectory to hop from tract to tract. Still, this method can provide quantitative information with which to visualize and study connectivity and continuity of neural pathways in the central and peripheral nervous systems in vivo, and holds promise for elucidating architectural features in other fibrous tissues and ordered media. Magn Reson Med 44:625–632, 2000. Published 2000 Wiley-Liss, Inc.†

Key words: MRI; DTI; DT; diffusion; tensor; human; brain; white matter; fiber; tract; trajectory; artifact; noise; curvature; torsion; bending

Diffusion tensor MRI (DT-MRI) (1) is the first noninvasive in vivo imaging modality with the potential to generate fiber-tract trajectories in soft fibrous tissues, such as nerves, muscles, ligaments, tendons, etc. (1–3). However, until recently this end could not be realized primarily for technical and mathematical reasons: First, the resolution and quality of diffusion-weighted images (DWIs) in vivo was not adequate for this demanding application. However, these problems have been ameliorated with the introduction of faster, more powerful gradients; single-shot diffusion-weighted echo-planar imaging (DW-EPI) sequences (4) with higher SNR and reduced motion artifacts (5); as well as schemes to reduce eddy current artifacts (6), and B_0 distortion (7). Second, the macroscopic fiber-tract direction field, $\boldsymbol{\varepsilon}_1(x,y,z)$, is obtained from measured DT-MRI data that is discrete, coarsely sampled, noisy, and voxel-averaged (8). Just as in hydrodynamics, it is difficult to construct fluid streamlines accurately from discrete, noisy, velocity field data (9); here it is difficult to follow a white matter fiber trajectory using discrete, noisy, direction field data. A methodology capable of generating a continuous, smooth representation of the measured DT-MRI data first had to be developed in order to ensure the reliability and robustness of DT-MRI fiber tractography. This mathematical framework is described in (10). Finally, a framework for following individual fiber tracts had to be developed, the underpinnings of which can be found in earlier works (3,8,11).

More recently, several groups have proposed tractography methods and have reported success in following fiber tracts, and even individual fascicles, over distances on a gross anatomical length scale (12–15). We do not attempt to compare and contrast our method or results with theirs. First, there are many new biologically relevant findings presented here and methodological issues raised in this work, so that including additional material would make this article unnecessarily long. Second, the steps involved in implementing some of these more recent tract-following schemes have, to date, only been outlined schematically, making it difficult to reproduce them, and thus to compare their findings fairly with ours.

The aims of this article are to 1) propose and describe a methodology to calculate continuous fiber-tract trajectories from discrete measured diffusion tensor MRI data; 2) present a general framework for testing the fidelity and robustness of this (and of other) fiber tract following schemes; 3) demonstrate that our method follows fiber tracts in the brain using in vivo DT-MRI data; 4) elucidate artifacts and inherent limitations of fiber tract following schemes that employ DT-MRI data; and 5) describe potential applications of DT-MRI fiber tractography.

THEORY

Evolution of Fiber Tract Trajectories

Previously, we proposed that a white matter fiber tract trajectory could be represented as a 3D space curve (3,8 11), i.e., a vector, $\mathbf{r}(s)$, parameterized by the arc length, s, of the trajectory.

The Frenet equation describing the evolution of $\mathbf{r}(s)$ is (16):

$$\frac{d\mathbf{r}(s)}{ds} = \mathbf{t}(s) \qquad [1]$$

where $\mathbf{t}(s)$ is the unit tangent vector to $\mathbf{r}(s)$ at s. These vectors are depicted in Fig. 1.

We also claimed that the normalized eigenvector, $\boldsymbol{\varepsilon}_1$, associated with the largest eigenvalue of the diffusion tensor, $\underline{\mathbf{D}}$, λ_1, lies parallel to the local fiber tract direction (1,2) in coherently organized white matter. To within acceptable experimental error, several groups have confirmed this to be true in the heart (17,18).

A key idea in our fiber tract following algorithm is to equate the tangent vector, $\mathbf{t}(s)$, and the unit eigenvector, $\boldsymbol{\varepsilon}_1$, calculated at position $\mathbf{r}(s)$:

$$\mathbf{t}(s) = \boldsymbol{\varepsilon}_1(\mathbf{r}(s)). \qquad [2]$$

[1]Section on Tissue Biophysics and Biomimetics, NICHD, Bethesda, Maryland.

[2]Mathematical and Statistical Computing Laboratory, CIT; NIH, Bethesda, Maryland.

[3]Department of Mathematics, Vanderbilt University, Nashville, Tennessee.

Grant sponsor: NSF; Grant number: DMS-9805483 (to A.A.).

*Correspondence to: Peter J. Basser, Ph.D., National Institutes of Health, Bldg. 13, Rm. 3W16, 13 South Drive, Bethesda, MD 20892-5772.
E-mail: pjbasser@helix.nih.gov

Received 27 January 2000; revised 2 June 2000; accepted 5 June 2000.

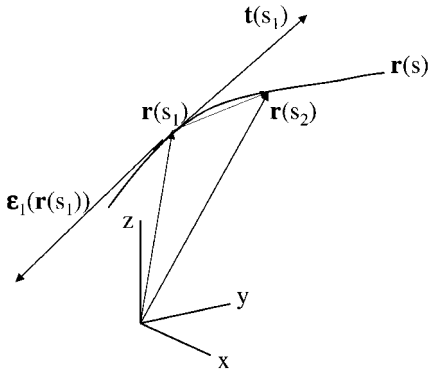

FIG. 1. Representation of a white matter fiber trajectory as a space curve, $\mathbf{r}(s)$. The local tangent vector, $\mathbf{t}(s_1)$, is identified with the eigenvector, $\boldsymbol{\varepsilon}_1(\mathbf{r}(s_1))$, associated with the largest eigenvalue of the diffusion tensor, $\underline{\mathbf{D}}$ at position $\mathbf{r}(s_1)$.

Therefore, combining Eqs. [1] and [2] we obtain:

$$\frac{d\mathbf{r}(s)}{ds} = \boldsymbol{\varepsilon}_1(\mathbf{r}(s)). \quad [3]$$

This system of three implicit (vector) differential equations is solved for the fiber tract trajectory subject to an initial condition:

$$\mathbf{r}(0) = \mathbf{r}_0 \quad [4]$$

which specifies a starting point on the fiber tract.

METHODOLOGY

The system of differential equations above, Eqs. [3] and [4], are implicit and forced. We could not find a general, analytical solution for $\mathbf{r}(s)$. Instead, numerical methods were employed.

Euler's Method

We use Euler's method (19) to see how such a solution might proceed. It is graphically outlined in Fig. 1. We choose a point on $\mathbf{r}(s)$, $\mathbf{r}(s_0)$, and evaluate the diffusion tensor there, $\underline{\mathbf{D}}(\mathbf{r}(s_0))$ (here we use the *continuous* representation of the tensor field at that point, as described elsewhere in the text). Then we approximate the position of a nearby point on $\mathbf{r}(s)$, $\mathbf{r}(s_1)$, by using a Taylor series expansion of $\mathbf{r}(s)$ about $\mathbf{r}(s_0)$: $\mathbf{r}(s_1) = \mathbf{r}(s_0) + \mathbf{r}'(s_0)\,(s_1 - s_0) + \ldots$. Since the slope of $\mathbf{r}(s_0)$ at s_0, $\mathbf{r}'(s_0)$, is assumed to be parallel to $\boldsymbol{\varepsilon}_1(\mathbf{r}(s_0))$, we can always find some small number α (with $0 < |\alpha| \ll 1$) such that $\mathbf{r}'(s_0)\,(s_1 - s_0) \sim \alpha\,\boldsymbol{\varepsilon}_1(\mathbf{r}(s_0))$. Once α is chosen, we can write:

$$\mathbf{r}(s_1) \sim \mathbf{r}(s_0) + \alpha\boldsymbol{\varepsilon}_1(\mathbf{r}(s_0)). \quad [5]$$

Thus, we can estimate $\mathbf{r}(s_1)$ from the values of $\mathbf{r}(s_0)$ and $\boldsymbol{\varepsilon}_1(\mathbf{r}(s_0))$. This procedure can now be repeated starting at the new point, $\mathbf{r}(s_1)$ …, and can be iterated to predict the location of discrete points along the fiber trajectory, $\mathbf{r}(s)$.

Runge-Kutta Method

While Euler's method is easy to explain and to implement, it is accurate only to 1st-order, and thus is susceptible to large accumulated errors and to numerical instabilities (19). Since our continuous representation of the diffusion tensor, $\underline{\mathbf{D}}(\mathbf{x})$ can furnish estimates of 2nd and higher derivatives of $\boldsymbol{\varepsilon}_1(\mathbf{x})$, it is prudent to use this information in a more robust and accurate numerical method to integrate these trajectories.

The 2nd-order or adaptive 4th-order Runge-Kutta methods are preferred to Euler's method to solve the system of differential equations above. One advantage of Runge-Kutta is that its estimates of higher derivatives of $\mathbf{r}(s)$ are more reliable. Another is that it is possible to employ adaptive step sizing to control the amount of error introduced in each integration step. Finally, a 4th-order Runge-Kutta scheme, described in Numerical Recipes (19), has been implemented as a callable subroutine within IDL (Research Systems, Boulder, CO), making it relatively easy to program.

Other Considerations in Fiber Tracking

One of the problems still to address is to assign the direction of the tangent vector in Eq. [2] consistently (20). This is complicated by the fact that the sign of $\boldsymbol{\varepsilon}_1$ is indeterminate, i.e., it can be positive or negative. Once the direction of the path of integration (i.e., the direction of the tangent to the curve) is first determined, $\boldsymbol{\varepsilon}_1$ should be chosen to point along the integration path consistently. This is done to avoid making erratic forward and backward steps as the path integration proceeds. To choose the tangent vector for the present step, we take the dot product between the eigenvector obtained in the previous step and the one calculated in the present step. If the result is positive (i.e., they point in the same direction) we preserve the sign of the new eigenvector; if the result is negative (i.e., they point in opposite directions), we swap its sign.

Not only must we choose the sign of $\boldsymbol{\varepsilon}_1$ consistently, but its direction as well. In each iteration above, we sort the eigenvalues of $\underline{\mathbf{D}}(\mathbf{x})$ according to their magnitude, associating the largest eigenvalue with $\boldsymbol{\varepsilon}_1$. However, background noise in DWIs can cause these eigenvalues to be misclassified (21), which consequently leads one to misclassify their corresponding eigenvectors (20). While at high SNR in coherent white matter tracts missorting eigenvalues is a relatively rare event, it occurs more frequently in less coherently organized white matter regions and at low SNR (22). If it occurs, $\boldsymbol{\varepsilon}_1$ no longer points along the true direction of the fiber (20), causing the trajectory suddenly to veer off course. To mitigate this problem, we check the coherence of fiber directions along the computed fiber tract and determine whether the local curvature (described below) between successive integration steps is large. If so, we stop the program, and report an error.

To help monitor the tract-following process, we also calculate intrinsic parameters of the trajectory, $\mathbf{r}(s)$, that characterize its torsional and bending motion within the imaging volume. The curvature, $\kappa(s)$, describes the propensity of $\mathbf{r}(s)$ to bend, while the torsion, $\tau(s)$, describes its

propensity to twist about the fiber axis. Both quantities can be readily calculated from the fiber tract trajectory, and its higher derivatives (23):

$$\kappa(s) = \frac{|d\mathbf{t}(s)|}{ds} = \frac{\left| d\left(\frac{\mathbf{r}'(s)}{|\mathbf{r}'(s)|} \right) \right|}{ds} \text{ and}$$

$$\tau(s) = \frac{\mathbf{r}'(s) \cdot (\mathbf{r}''(s) \times \mathbf{r}'''(s))}{\kappa(s)^2} \text{ for } \kappa(s) \neq 0. \quad [6]$$

The curvature and torsion can also be used as MRI stains that elucidate novel intrinsic geometric features of the fiber trajectory (3).

We stop following fibers for four reasons: 1) the tract reaches the boundary of the imaging volume; 2) the tract reaches a region with low diffusion anisotropy (lattice index < 0.1); 3) the radius of curvature of the tract is smaller than approximately two voxels; and 4) the eigenvector that is the most collinear is not the same as the eigenvector associated with the largest eigenvalue.

Algorithms to Approximate or Interpolate a Tensor Field

We recently developed a mathematical framework and methodology to obtain a continuous representation of $\boldsymbol{\varepsilon}_1(\mathbf{x})$, which is necessary to integrate the differential equations above. We do this by first generating a continuous approximation of $\underline{\mathbf{D}}(\mathbf{x})$, and then calculating $\boldsymbol{\varepsilon}_1(\mathbf{x})$ from it. The underpinnings of this approach have been described elsewhere (10,24). There are two types of continuous representations of tensor field data that we use in this study: approximation and interpolation (10). Approximation involves finding a set of B-spline functions that smoothly "fits" the noisy discrete experimental data in a least-squared sense, just as linear regression fits a line to a set of discrete noisy data points. We use approximation in our tract-following scheme to obtain a noise-reduced, smoothed, continuous representation of the experimental diffusion tensor field data, from which a smooth representation of the fiber direction field can be obtained. Interpolation involves finding a continuous representation, using an appropriate set of B-spline functions that are constrained to pass through all of the measured noisy, discrete tensor data. We see below that using smoothed approximated data rather than noisy interpolated data results in improved performance of our tract-tracing scheme.

Diffusion Tensor Field Templates

To test the fidelity and robustness of the fiber-following algorithm, we synthesized a family of analytical 3D $\underline{\mathbf{D}}(\mathbf{x})$ maps whose fiber tract direction fields possess characteristics or patterns seen in vivo, or exhibit peculiar mathematical features or pathologies. The former include uniform (white matter) fiber tracts in isotropic (gray matter) domains, or fiber tracts that circulate, cross or "kiss," merge or branch, bulge or neck, terminate or kink. The latter include, fiber tract trajectories that oscillate periodically or variably (e.g., "chirp"). These tensor fields are synthesized from piecewise-continuous functions and then discretely sampled as described in Ref. 8. To assess noise immunity of the fiber tract-following method, Monte Carlo simulations of DT-MRI experiments were performed using these tensor field patterns. In each voxel, Rician RF noise (25,26) was added to an ideal NMR signal that is calculated from the prescribed diffusion tensor there, and from the gradient sequence, as described previously (21). This procedure results in noisy diffusion-weighted MRIs (DWIs) (21) from which we estimate a discrete, noisy diffusion tensor field using methods described previously (27–29). In this way we can vary the SNR systematically to study the effect of background noise on the variability of the fiber direction field itself, and to assess the ability of the fiber tractography scheme to follow fibers faithfully. To assess the reliability and reproducibility of this tract-following method, we construct noisy realizations of a uniform anisotropic diffusion tensor field within a straight white matter fiber tract. A straight, synthetically generated fiber tract, 128 voxels long and 5 voxels in diameter, was constructed for this purpose. We launch trajectories from a particular point along the tract and follow them until they intersect the fiber boundary, at which point we deem that the tract-following method fails.

DT-MRI Methods

Healthy volunteers were scanned using a 1.5 T GE Signa Horizon EchoSpeed equipped with a 2.2 G/cm gradient set, according to an approved NIH clinical protocol. A set of DWIs were acquired in six isotropically distributed directions, using an interleaved, spin-echo, echo-planar sequence, employing navigator echo correction, as described in (30). DWI parameters were as follows: FOV = 22 cm, TE = 78 ms, TR $>$ 5 sec with cardiac gating, voxel size = $3.5 \times 1.75 \times 1.75$ mm, data matrix = 128×128. The strength of diffusion weighting as measured by Trace($\underline{\mathbf{b}}$) (where $\underline{\mathbf{b}}$ is the b-matrix (27–29,31) calculated for each DWI) was varied from approximately 0 to 1000 s/mm^2.

An effective diffusion tensor was calculated in each voxel according to (27,29,31). Maps of useful MR parameters calculated from the diffusion tensor, such as Trace($\underline{\mathbf{D}}$), diffusion anisotropy measures (such as the relative anisotropy (RA), the fractional anisotropy (FA) (32) and the lattice index (21)), diffusion ellipsoid images, etc. (1,2) all provide information to evaluate fiber tract architecture in the brain (22).

RESULTS

Synthetic Data

To identify possible artifacts and/or limitations of the tract-following method, we constructed continuous tensor fields described above. Figure 2 shows a synthetically generated fiber map whose primary eigenvectors are circumferentially orientated. The object is constructed within a $128 \times 128 \times 1$ imaging volume. Trajectories are computed in each ring using the Euler method with a 0.1 voxel step size. In each case, starting at a particular point on a ring, we attempt to follow a fiber tract for 20 revolutions. Tract-following is most accurate in the ring with the largest diameter, or smallest radius of curvature, but de-

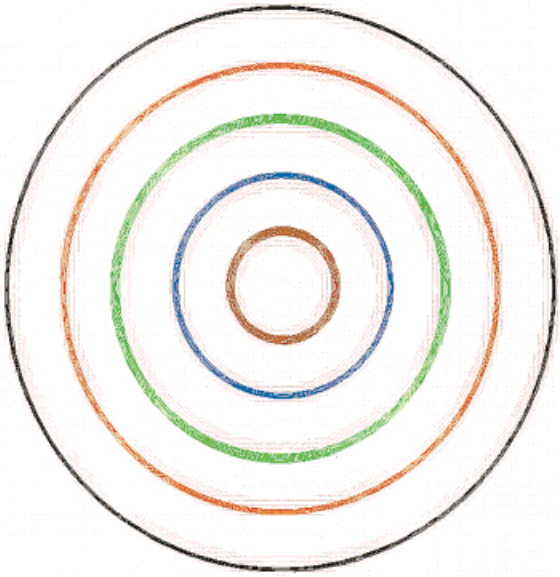

FIG. 2. Fiber tract trajectories, **r**(s), calculated from a synthetic diffusion tensor field consisting of concentric rings in which the primary eigenvector, $\varepsilon_1(\mathbf{r}(s))$, is oriented circumferentially. Fiber tract trajectories, depicted in different colors, are launched from a single point in the middle of each ring, and followed for 20 revolutions. Accuracy degrades as the radius of curvature decreases.

grades as ring diameter decreases, as evidenced by the increasing width of the trajectories. In the innermost ring, following was terminated after only 17 revolutions when the trajectory intersected the perimeter of the ring.

Generally, we find that the Euler method can be used to follow fiber tracts provided that the step size is chosen to be significantly smaller than the minimum radius of curvature along the entire length of the tract. Operationally, the step size can be decreased until the fiber trajectory becomes stable and reproducible. In this application, it is usually sufficient to choose $\alpha < (0.05 \times L)$, where L is a voxel dimension. Still, an adaptive Runge-Kutta or Gear's method is preferred to Euler's method for reasons given above.

To identify possible artifacts introduced by interpolating or approximating discrete noisy tensor data, we sampled continuous tensor fields at discrete points, adding Rician noise in the manner described in the Methods section. We then obtained an interpolated or approximated continuous tensor field representation of the sampled data from the noisy DWIs. Figure 3a shows trajectories obtained by interpolating the noisy data; Fig. 3b shows trajectories obtained by approximating the noisy data. The SNR of both simulations is the same, 10; and $\lambda_1 : \lambda_2 : \lambda_3 = 2 : 1 : 1$.

The performance of the tract-following algorithm is poorer when using interpolated noisy data rather than smoothed approximated data at the same SNR. Similar results were found in other synthetic datasets and at all other SNRs tested. Most of the trajectories using interpolated data failed to traverse the entire length of the fiber.

Tensor fields were constructed to identify possible artifacts introduced when fibers kiss, cross, merge, branch,

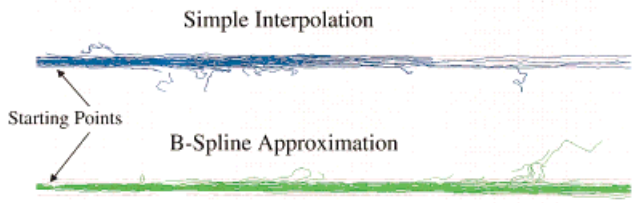

FIG. 3. Following straight fiber tracts. Simulated fiber tract trajectories, **r**(s), are calculated from 50 different noise realizations of synthetic diffusion tensor fields (SNR = 10; λ_1:λ_2:λ_3 = 2:1:1). Tracts are launched from a single point within a bundle of straight fibers. Tract following is less accurate and robust when using interpolated (top) rather than approximated (bottom) diffusion tensor data.

bulge, or neck. Two such fields are represented in Fig. 4a,b. Crossing fibers are depicted in Fig. 4a, while "kissing" fibers are depicted in Fig. 4b. In Figure 4a trajectories were released from a small ROI and allowed to follow fibers in both directions. Again, the diffusion tensor field was approximated using the methods described above with a scale factor of 0.75. Here, fibers released on one branch are reflected at the plane of symmetry. However, as SNR decreases one can also observe fibers occasionally crossing the plane of symmetry, as in Fig. 4b. In Fig. 4b trajectories were released from a small ROI in the left ring. In some cases, the fiber trajectory crosses from the left to the right ring. The tensor approximation scheme, which tries to establish continuity of the tensor field, including at singularities, chooses solutions that tend to keep fibers separated.

Human Brain Data

Figure 5 shows fiber tract trajectories, **r**(s), computed from in vivo human DT-MRI data by launching trajectories from an ROI located at the center of the splenium of the corpus callosum on a single slice. Tracts are followed in both

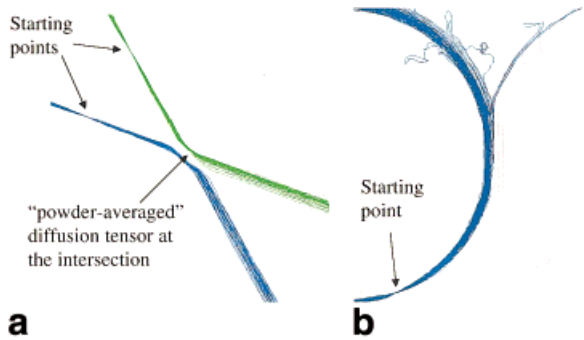

FIG. 4. Artifacts in fiber following due to singularities in the diffusion tensor field. **a,b:** Crossing and "kissing" fibers tracts, respectively. **a** shows a bias against fibers crossing the plane of symmetry (SNR=20; λ_1:λ_2:λ_3 = 3:1:1). **b** shows that occasionally noise can cause trajectories to jump from one tract to another near a singularity (SNR=20; λ_1:λ_2:λ_3 = 2:1:1).

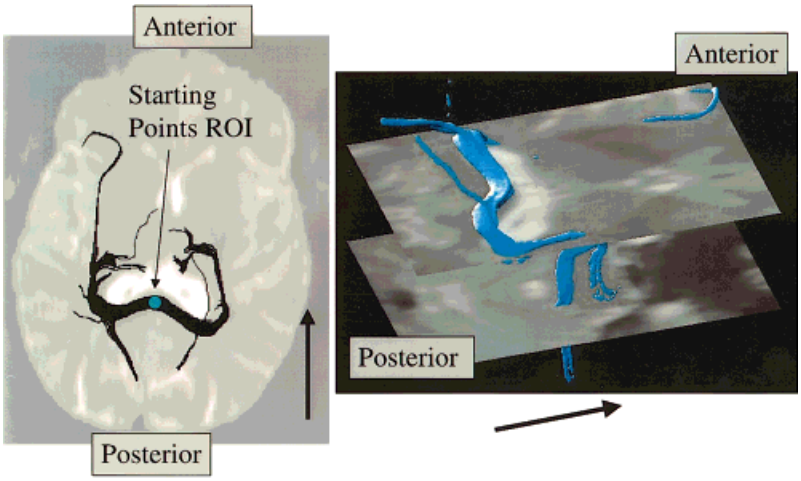

FIG. 5. Fiber tract trajectories, **r**(s), computed in the corpus callosum using in vivo human DT-MRI data. Trajectories were "launched" from a ROI located at the center of the splenium of the corpus callosum at its intersection with the interhemispheric plane. **a:** A projection of these computed trajectories onto a T_2-weighted amplitude image of the brain at the level of the ROI. **b:** 3D rendering of the computed trajectories superimposed on a T_2-weighted amplitude images of the brain at a level below the ROI.

directions. Figure 5a shows a projection of these computed trajectories onto a T_2-weighted amplitude image of the brain at the level of the selected ROI. Figure 5b shows a 3D rendering of the computed trajectories with T_2-weighted amplitude images displayed at slices below the ROI. Fiber trajectories within the body of the corpus callosum are consistent with the known anatomy of this structure. Fiber trajectories continuing beyond the external margins of the lateral ventricles appear to follow anatomically defined tracts (external capsule and pathways projecting to the occipital lobe); however, establishing if the apparent continuity of callosal fibers into these tracts is a true anatomical feature requires validation by histological techniques.

Figure 6a also shows a 3D rendering of computed trajectories from human DT-MRI data. In this figure we map long projection pathways by launching trajectories from ROIs positioned in the internal capsule at the level of the globus pallidum, in the pyramidal tract at the level of the cerebral peduncles and the pons, and in the ascending sensory fibers (lemniscus medialis) at the level of the pons. Tracts are followed in both directions. Only regions within the imaging volume for which the lattice anisotropy index is greater than 0.3 are used. This is to ensure that fiber tracts are launched from regions of coherently organized white matter. Figure 6b shows a projection of these computed trajectories. This figure is obtained from the previous one by counting the number of fibers passing through each voxel and assigning an intensity to each voxel which is proportional to this number. This distribution is then projected onto the plane of view in a manner similar to the way a maximum intensity projection (MIP) image would be produced. The pathways highlighted in this figure are consistent with the known gross anatomy of the long projection pathways. Interestingly, motor fiber trajectories originating from the ROI in the cerebral peduncle usually continue superiorly up to the cortex, while sensory fiber trajectories from the ROI in the lemniscus medialis do not. This is consistent with the notion that sensory fibers project to the thalamus, while motor fibers of the pyramidal tract descend uninterrupted from the cortex to the brainstem and the spine.

Figure 7 shows a 3D rendering of computed trajectories within the corpus callosum. This figure is obtained by launching trajectories from a multislice ROI located in the body of the corpus callosum in the proximity of the midline. We require that the lattice anisotropy index of all voxels within the ROI is greater than 0.6 to ensure that fiber tracts are being launched from regions of coherently organized white matter with no partial volume contamination from CSF. Tracts are also followed in both directions. The majority of fiber trajectories from the corpus callosum continue upward toward the cingular cortex.

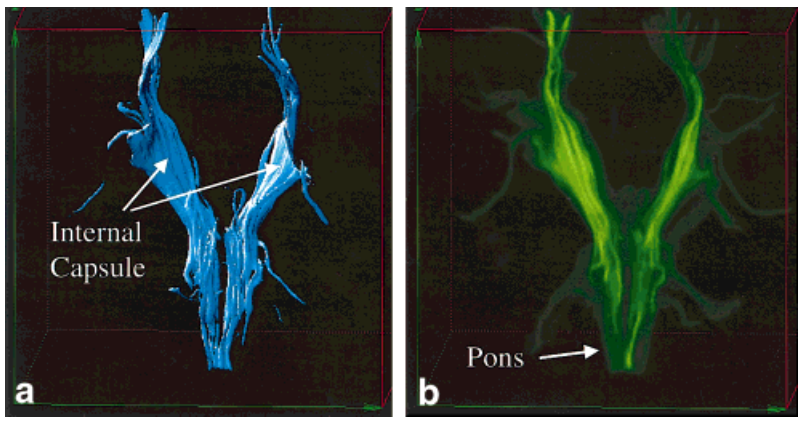

FIG. 6. 3D rendering of computed trajectories of long projection pathways using in vivo human DT-MRI data. Trajectories are launched from ROIs in the internal capsule at the level of the globus pallidum, in the pyramidal tract at the level of the cerebral peduncles and the pons, and in the ascending sensory fibers (lemniscus medialis) at the level of the pons. Tracts are followed in both directions. **a:** Surface shaded rendering of these pathways. **b:** A fiber tract density map of these computed trajectories in which the image intensity is proportional to the number of fibers passing through each voxel. This distribution is then projected onto the plane of view, as in a MIP image.

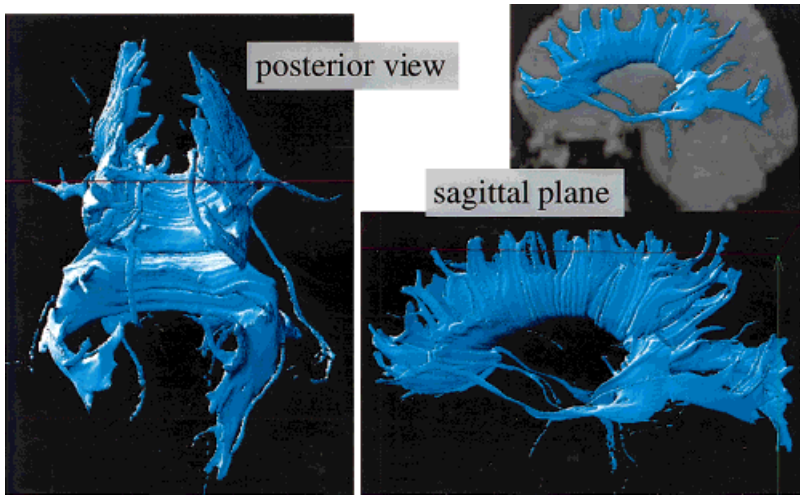

FIG. 7. 3D rendering of computed trajectories within the corpus callosum. Trajectories are launched in both directions from a multislice ROI located in the body of the corpus callosum in the proximity of the midline. The majority of fiber trajectories continue upward toward the cingular cortex. The cingulum is the thin bundle running anteroposteriorly above the corpus callosum (see arrows in figure showing posterior view).

Interestingly, the cingulum can be clearly seen as a relatively thin bundle running anteroposteriorly above the corpus callosum (arrows in Fig. 7a). Considering that the ROI from which the trajectories originate does not include any portion of the cingulum, its inclusion implies that the tractography algorithm had found a connection between the callosal and cingular fibers. Whether this is an important anatomical finding or just an artifact requires further study.

DISCUSSION

Obstacles to DT-MRI Tractography

There are several obstacles to elucidating fiber tract trajectories quantitatively. First, there is presently no "gold standard" for in vivo fiber tractography (33). In fact, DT-MRI is the only method of which we are aware that permits the calculation and visualization of fiber tract trajectories in optically turbid tissue in vivo (and was developed, in part, to address this unmet need). In vitro validation of fiber tract direction fields obtained by DT-MRI has been attempted histologically (17,18). Of course, sample registration, dissection, freezing, dehydration, fixation, microtoming, thawing, etc., each can alter tissue microstructure and microanatomy and introduce geometric distortion in the histological sample. Therefore, great care is required to compare fiber directions in living tissue and a fixed specimen prepared from it. Thus, the diffusion tensor field templates take on greater importance in helping us to validate fiber-tracking methods that use DT-MRI data.

All of the usual artifacts and problems in DWI experiments can adversely affect fiber tracking in predictable ways. Misregistration of DWIs caused by eddy currents, ghosting due to motion artifacts, and signal loss due to susceptibility variations could all affect the computed trajectories. However, many of these problems can be mitigated using well-established correction schemes. The use of isotropic voxels is recommended to ensure that the accuracy of the tractography scheme is independent of fiber direction.

The diffusion tensor used to measure the fiber tract direction is a voxel-averaged quantity. In voxels containing anisotropic fibrous tissues having a uniform fiber direction, the eigenvector associated with the largest eigenvalue of the effective diffusion tensor provides an unbiased estimate of the microscopic fiber field direction vector (34). However, if there is a nonuniform distribution of fiber directions then the NMR signal we measure depends in a complicated way on structure and architecture of the tissue (22). Then the eigenvector associated with the largest eigenvalue of the effective diffusion tensor only corresponds to a consensus average fiber direction within the voxel. There, "powder averaging" of the microscopic $\mathbf{D}$-field occurs (21,22). If the voxel contains curved fiber tracts, then using smaller voxels can ameliorate this problem. If the voxel contains two or more distinct populations of interdigitating fibers, then reducing voxel size does not remedy the problem (21). This problem becomes even more severe at singularities in the microscopic direction field (3,8,35), for example, where fiber tracts cross or "kiss," or branch or merge. As we have shown above, within singular regions fiber tract trajectories calculated from the original or smoothed direction field may fail to follow the true fiber tract trajectory. While recently proposed novel methods of Bossart et al. (36) and Tuch et al. (37) identify two nonexchanging populations of water molecules that diffuse anisotropically within a voxel, they still do not address how such fibers are connected within a singular region. Do they kiss, cross, or is their pattern some combination of both? A future challenge is to circumvent powder-averaging effects by employing additional a priori anatomical information about the distribution of fiber tract directions and structural information about tissue composition within these voxels, so one can reconstruct white matter fiber tract trajectories in complex structures such as the ventral internal capsule, the optic chiasm, the pyramidal tract, and in other white matter structures where the fiber direction field may not be uniform.

Moreover, at points where there are discontinuities in **r**(s), or in its derivatives (such as where there are transections, or at points where the fiber tract is kink), tractography methods that "regularize" (13) the fiber trajectory may artifactually introduce fiber continuity there. This would apply particularly to schemes that introduce "memory" or which model the tract as having some inherent "bending stiffness." Generally, our ability to observe wiggles, gaps, or discontinuities in fiber tracts depends on a number of variables, such as the radius of the fiber, the width of the gap, the voxel size, the scale of the smoothing window, the background noise level, and the algorithm used. If we choose our smoothing window to be too large, it is possible to smooth over a transected fiber so it will appear continuous.

Other artifacts may be introduced when smoothing a noisy diffusion tensor field. Generating a continuous approximation to the tensor field can introduce phantom connections between tracts which do not exist anatomically. In an attempt to make the field continuous within white matter regions, distinct fiber tracts that may be separated from each other by a voxel or two may be bridged or merged. In this way, "blebs" on different neighboring tracts can coalesce to form an artifactual connection or nexus, which can cause the computed trajectory to "jump" tracts. The larger the smoothing window chosen for the tensor approximation, the greater the likelihood of this problem occurring.

Not remediating noise in the DWIs can also have adverse consequences, since it can cause one to sort eigenvectors incorrectly (20). As described above, this results in a sudden 90° deviation in the computed trajectory, which causes the trajectory to "jump" to another tract (20). Noise in DT-MRI data also introduces scatter in the distribution of the eigenvectors (38), even when the eigenvalues are sorted correctly. A fiber-tracking scheme that follows noisy (interpolated) eigenvector data will eventually meander away from the true trajectory. Moreover, owing to noise, MRI data obtained under the same experimental conditions is not expected to produce identical trajectories. It is troubling that noise-induced artifacts described above can produce anatomically plausible but erroneous nerve trajectories and potentially false connections.

In our in vivo studies, we observed significant differences in both the geometry (i.e., shape) and *topology* (i.e., branching pattern) of fiber tract trajectories when we perturb their starting points slightly (i.e., on a length scale smaller than an individual voxel). A direct consequence is that one could infer an altogether different "connectivity" pattern and biological function of adjacent tracts. Whether this observation is anatomically correct is not ascertainable at this time.

With the many concerns raised and caveats described above about fiber tractography using DT-MRI data, one should view reports of newly discovered white matter fiber pathways within the brain with healthy skepticism, as these findings could easily be due to one of the many artifacts described above. In evaluating any DT-MRI fiber tractography study, one should be convinced that all possible artifacts were considered, assessed, controlled for, and remedied.

Applications of DT-MRI Tractography

DT-MRI tractography should improve our understanding of brain pathology, particularly of white matter abnormalities occurring in closed head trauma, stroke, etc. It is also likely that DT-MR fiber tractography will be used to follow trajectories of the peripheral nervous system (PNS). There, branching patterns are simpler to follow than in the CNS, and the distances over which fiber direction and architectural organization are uniform are greater. Changes in diameter of injured nerves, and localized bulging or necking of fiber tracts, might also be detectable using this approach. Radial displacement of a computed fiber tract could indicate a region of local nerve swelling or focal compression. A localized net displacement of a computed fiber tract could indicate nearby pathological tissue regions.

Finally, DT-MRI fiber tractography methods could be applied to other fibrous tissues, such as the heart, whose fiber directional pattern and organization is critical in following its normal development and diagnosing disease. Tractography adds new information to what is provided by the computed fiber direction field (39).

Methods to visualize fiber tracts that employ contrast agents, such as manganese (40), are complementary with DT-MRI fiber tractography and could be used in conjunction with it.

Concluding Remarks

Here we have reduced the complex task of tracing the trajectory of white matter fiber tracts in vivo to solving a system of ordinary differential equations that employ measured DT-MRI data. The primary applications of DT-MRI fiber tractography are in establishing 1) whether and how different regions of the brain that perform critical processing tasks are connected via large fiber pathways (8,35), and 2) whether a white matter fiber tract is continuous (8). The first problem entails determining whether two points (or two different ROIs) can be joined by one or more fiber-tract trajectories. The second problem entails following a trajectory from one point along a fiber to its terminus. The latter is an initial-value problem; the former is a two-point boundary value problem.

Coherently oriented white matter tracts, such as the corpus callosum, can be followed provided that the artifacts brought to light above are carefully assessed and systematically addressed.

DT-MRI fiber-tractography can provide unique quantitative and qualitative information to aid in visualizing and in studying fiber tract architecture in the brain and in other fibrous tissues. It has the potential to advance our understanding of connectivity and continuity in the central and peripheral nervous system in vivo.

REFERENCES

1. Basser PJ, Le Bihan D. Fiber orientation mapping in an anisotropic medium with NMR diffusion spectroscopy. In: Proceedings of the 11th Annual Meeting of the SMRM, Berlin, 1992. p 1221.
2. Basser PJ, Mattiello J, Le Bihan D. MR diffusion tensor spectroscopy and imaging. Biophys J 1994;66:259–267.

3. Basser PJ. New histological and physiological stains derived from diffusion-tensor MR images. Ann NY Acad Sci 1997;820:123–138.
4. Turner R, Le Bihan D. Single shot diffusion imaging at 2.0 Tesla. J Magn Reson 1990;86:445–452.
5. Ordidge RJ, Helpern JA, Qing ZX, Knight RA, Nagesh V. Correction of motional artifacts in diffusion-weighted MR images using navigator echoes. Magn Reson Imaging 1994;12:455–460.
6. Jezzard P, Barnett AS, Pierpaoli C. Characterization of and correction for eddy current artifacts in echo planar diffusion imaging. Magn Reson Med 1998;39:801–812.
7. Jezzard P, Balaban RS. Correction for geometric distortion in echo planar images from B0 field variations. Magn Reson Med 1995;34:65–73.
8. Basser PJ. Fiber-tractography via diffusion tensor MRI (DT-MRI). In: Proceedings of the 6th Annual Meeting ISMRM, Sydney, Australia, 1998. p 1226.
9. Yeung P, Pope S. An algorithm for tracking fluid particles in numerical simulations of homogeneous turbulence. J Comput Phys 1988;79:373–416.
10. Aldroubi A, Basser PJ. Reconstruction of vector and tensor fields from sampled discrete data. In: Baggett LW, Larson DR, editors. Contemporary mathematics. Providence, RI: AMS; 1999. p 1–15.
11. Basser PJ, Roth BJ. Stimulation of a myelinated nerve axon by electromagnetic induction. Med Biol Eng Comput 1991;29:261–268.
12. Jones DK, Simmons A, Williams SC, Horsfield MA. Non-invasive assessment of axonal fiber connectivity in the human brain via diffusion tensor MRI. Magn Reson Med 1999;42:37–41.
13. Poupon C, Clark CA, Frouin V, Bloch I, Bihan DL, Mangin J-F. Tracking white matter fascicles with diffusion tensor imaging. In: Proceedings of the 8th Annual Meeting ISMRM, Philadelphia, 1999. p 325.
14. Mori S, Crain BJ, Chacko VP, van Zijl PC. Three-dimensional tracking of axonal projections in the brain by magnetic resonance imaging. Ann Neurol 1999;45:265–269.
15. Lori NF, Cull TS, Akbudak E, Snyder AZ, Shimony JS, Burton H, Raichle ME, Conturo TE. Tracking neuronal fibers in the living human brain with diffusion MRI. In: Proceedings of the 8th Annual Meeting, ISMRM, Philadelphia, 1999. p 324.
16. Frenet F. Sur les courbes á doublette courbure. Toulouse, France, 1847.
17. Scollan DF, Holmes A, Winslow R, Forder J. Histological validation of myocardial microstructure obtained from diffusion tensor magnetic resonance imaging. Am J Physiol 1998;275:H2308–2318.
18. Hsu EW, Muzikant AL, Matulevicius SA, Penland RC, Henriquez CS. Magnetic resonance myocardial fiber-orientation mapping with direct histological correlation. Am J Physiol 1998;274:H1627–1634.
19. Press WH, Teukolsky SA, Vetterling WT, Flannery BP. Numerical recipes in C. Cambridge: Cambridge University Press; 1992.
20. Basser PJ, Pajevic S. Statistical artifacts in DT-MRI data caused by background noise. Magn Reson Med 2000;44:41–50.
21. Pierpaoli C, Basser PJ. Toward a quantitative assessment of diffusion anisotropy. Magn Reson Med 1996;36:893–906 [erratum Magn Reson Med 1997;37:972].
22. Pierpaoli C, Jezzard P, Basser PJ, Barnett A, Di Chiro G. Diffusion tensor MR imaging of the human brain. Radiology 1996;201:637–648.
23. Struik DJ. Lectures on classical differential geometry. New York: Dover; 1961.
24. Basser PJ, Pajevic S, Pierpaoli C, Aldroubi A, Duda J. Fiber-tractography in human brain using diffusion tensor MRI (DT-MRI). In: Proceedings of the 8th Annual Meeting ISMRM, Denver, 2000. p 784.
25. Henkelman RM. Measurement of signal intensities in the presence of noise in MR images. Med Phys 1985;12:232–233.
26. Gudbjartsson H, Patz S. The Rician distribution of noisy MRI data Magn Reson Med 1995;34:910–914 [erratum Magn Reson Med 1996; 36:332].
27. Basser PJ, Mattiello J, Le Bihan D. Estimation of the effective self-diffusion tensor from the NMR spin echo. J Magn Reson B 1994;103: 247–254.
28. Mattiello J, Basser PJ, Le Bihan D. Analytical expression for the b matrix in NMR diffusion imaging and spectroscopy. J Magn Reson A 1994;108:131–141.
29. Mattiello J, Basser PJ, Le Bihan D. The b matrix in diffusion tensor echo-planar imaging. Magn Reson Med 1997;37:292–300.
30. Virta A, Barnett A, Pierpaoli C. Visualizing and characterizing white matter fiber structure and architecture in the human pyramidal tract using diffusion tensor MRI. Magn Reson Imaging 1999;17:1121–1133.
31. Mattiello J, Basser PJ, Le Bihan D. Analytical calculation of the b matrix in diffusion imaging. In: Le Bihan D, editor. Diffusion and perfusion magnetic resonance imaging. New York: Raven Press; 1995. p 77–90.
32. Basser PJ, Pierpaoli C. Microstructural and physiological features of tissues elucidated by quantitative-diffusion-tensor MRI. J Magn Reson B 1996;111:209–219.
33. Crick F, Jones E. Backwardness of human neuroanatomy. Nature 1993; 361:109–110.
34. Pajevic S, Basser PJ. Non-parametric statistical analysis of diffusion tensor MRI data using the bootstrap method. In: Proceedings of the 8th Annual Meeting ISMRM, Philadelphia, 1999. p 1790.
35. Pierpaoli C, Barnett A, Virta A, Penix L, Chen R. Diffusion MRI of Wallerian degeneration. A new tool to investigate neural connectivity in vivo? In: Proceedings of the 6th Annual Meeting ISMRM, Sydney, Australia, 1998. p 1247.
36. Bossart EL, Inglis BA, Buckley DL, Wirth ED III, Mareci TH. Multiple component diffusion tensor imaging in excised fixed CNS tissue. In: Proceedings of the 8th Annual Meeting ISMRM, Philadelphia, 1999. p 328.
37. Tuch DS, Weiskoff RM, Belliveau JW, Wedeen VJ. High angular resolution diffusion imaging of the human brain. In: Proceedings of the 8th Annual Meeting ISMRM, Philadelphia, 1999. p 321.
38. Basser PJ. Quantifying errors in fiber direction and diffusion tensor field maps resulting from MR Noise. In: Proceedings of the 5th Scientific Meeting ISMRM, Vancouver, 1997. p 1740.
39. Garrido L, Wedeen VJ, Kwong KK, Spencer UM, Kantor HL. Anisotropy of water diffusion in the myocardium of the rat. Circ Res 1994;74:789–793.
40. Pautler RG, Silva AC, Koretsky AP. In vivo neuronal tract tracing using manganese-enhanced magnetic resonance imaging. Magn Reson Med 1998;40:740–748.